Journal of Sound and Vibration (2002) **256**(2), 227–248
doi:10.1006/jsvi.2001.4203, available online at http://www.idealibrary.com on IDEAL®

AEROELASTIC FLUTTER OF CIRCULAR ROTATING DISKS: A SIMPLE PREDICTIVE MODEL

H.-R. KIM

Optical Disc Drive Division, Samsung Electronics Co., 416 *Maetan*-3 *Dong, Paldal-Gu, Suwon* 442-742, *Korea*

AND

A. A. RENSHAW

Department of Mechanical Engineering, Columbia University, Mail Code 4703, *New York, NY* 10027, *U.S.A.*

(*Received* 19 *December* 2000, *and in final form* 10 *December* 2001)

This paper is an attempt to predict aeroelastic flutter of a rotating disk in an unbounded fluid. In the first part of the paper, the linear vibration of a rotating, potential fluid driven by transverse, harmonic motion of a rotating disk is solved. We extend the existing solution for a rigid disk to include flexible disks and compare alternative numerical evaluation schemes. Our principal interest in this problem is the identification of possible physical mechanisms for aeroelastic flutter. In the forced vibration problem considered here, fluid rotation renders the governing equations hyperbolic for low-frequency oscillation. As a result, the fluid motion may be discontinuous along the two characteristics that emanate from the rim of the disk. These discontinuities suggest the presence of previously unrecognized boundary layers near the rim of the disk that may be important for aeroelastic flutter. This idea is used to develop a simple mathematical model for predicting aeroelastic flutter. The model and its dependence on the dimensionless parameters describing the system are derived from first principles except for the compressible boundary layer, which is described by a simple function whose magnitude is empirically determined by fitting experimental data. Although the model is simple, its predictions are quantitatively similar to the experimental evidence and gives analytic predictions of aeroelastic flutter that are within an order of magnitude of the experimental values.

1. INTRODUCTION

Aeroelastic flutter of a rotating disk is an unstable coupling between the disk and the surrounding air that occurs at high rotation speeds [1–3]. If a thin, uniform, circular disk is spun in air below the flutter speed, the peak to peak transverse oscillations of the disk are below or on the order of the thickness of the disk. Above the flutter speed, the disk undergoes large, fluttering, transverse vibrations whose amplitudes are at least an order of magnitude greater than the thickness of the disk. The importance of aerodynamic coupling can be demonstrated by spinning the disk in a partial vacuum. The reduced fluid density increases the speed at which self-excited oscillations first occur.

Presently, for disks in an unbounded fluid, there is poor agreement between experimental aeroelastic flutter data and the analytical predictions based on classical aeroelasticity [2, 3]. In addition, the experimental evidence indicates that the rim Mach number is important even though it is small ($< 0{\cdot}3$) [3]. Classical aeroelasticity predicts that compressibility

0022-460X/02/$35.00

effects should be negligible at these Mach numbers. This discrepancy with experimental results suggests that some physical mechanism essential to aeroelastic flutter is missing from the classical aeroelasticity models.

Other researchers have proposed models incorporating different forms of rotating damping [4–6]. This kind of damping frequently occurs in hydrodynamic lubrication theory when analyzing disks with small transverse clearances such as floppy disks [7–9]. Hansen *et al.* [5] and Kim *et al.* [6] argue that this form of damping can be found in disks rotating in an unbounded fluid and provide an experimental measurement technique for predicting aeroelastic flutter based on this idea. However, they do not provide any theoretical model for predicting flutter.

In contrast to aeroelastic flutter, a great deal is understood about the viscous flow induced by a rigid rotating disk [10–12]. The existence of a viscous boundary layer near a rotating disk has been firmly established, and its structure in the laminar, turbulent, and transition regimes has been documented. Many of these studies use disks with approximately the same diameter and rotation speed as those reported here. It is probable that proper modelling of the viscous boundary layer is required to derive a first principles model of aeroelastic flutter. However, the connection between the viscous flow field results and aeroelastic flutter is far from clear. For example, Kohama [12] observed 34 spiral vortices across an annular region of the disk in the transition region between laminar and turbulent flow, while experimental results have observed unstable aeroelastic flutter modes with only 3 to 4 nodal diameters [2]. This discrepancy suggests that spiral vortices may not be important to aeroelastic flutter since, in a linear theory, an excitation with an angular periodicity of 34 cannot excite a mode with an angular periodicity of 3 or 4.

This paper proposes a model for predicting aeroelastic flutter in an unbounded fluid. In the first part of the paper, our aim is to examine a physical mechanism that may be important for flutter. To do so, we examine a classical fluid dynamics problem: the linear vibration of a rotating, potential fluid driven by transverse, harmonic motion of a rotating disk [13]. We extend the known solution for a rigid disk to include motion of a flexible disk. A closed-form solution in terms of quadratures is derived and alternative numerical evaluation procedures are compared. The results indicate that low-frequency disk vibration can cause the flow field to be discontinuous across the characteristics that emanate from the rim of the disk. These discontinuities suggest the presence of previously unrecognized boundary layers near the rim of the disk that may be important for aeroelastic flutter.

We use the idea of a compressible boundary layer near the rim of a rotating disk to develop a simple predictive model. The model developed here and its dependence on the dimensionless parameters describing the system are derived from first principles except for the effect of the compressible boundary layer, which is described by a simple function whose magnitude is determined empirically using experimental data collected here and described in the literature. Although the model is simple, its predictions are within an order of magnitude of experimental values for a broad range of data. Furthermore, the predictions are quantitatively similar to the experimental evidence in a number of respects. The model gives a method for predicting aeroelastic flutter analytically and sets the stage for more refined modelling efforts.

We note that the proposed model is for predicting aeroelastic flutter, not explaining it. There are serious defects with the model proposed: it does not tie in the literature on disk boundary layer flow; the aerodynamic coupling is fit from experimental data rather than calculated a priori; and the mathematical modelling is at times *ad hoc*, especially in transferring compressibility from the equations describing the fluid to the boundary conditions coupling the fluid with the plate. These are weaknesses of the model, which the

authors readily acknowledge. However, despite these broad simplifications, the resulting model gives reasonably accurate predictions.

2. A MOTIVATING EXAMPLE

We begin by examining a classical forced vibration problem whose solution motivates new modelling strategies for aeroelastic flutter.

A thin, axisymmetric, circular disk of outer radius R_o spins about its axis of symmetry at a constant angular speed Ω. The disk is surrounded by an inviscid, incompressible fluid undergoing solid body rotation with the disk. The problem is to determine the linear, harmonic vibration of the fluid when the transverse deflection of the disk, $W(T, R, \theta)$, is driven at frequency ω^* such that

$$W = \frac{-\mathrm{i}}{\omega^*} \mathrm{e}^{\mathrm{i}(\omega^* T \pm n\theta)} F(R), \tag{1}$$

where (R, θ) are polar co-ordinates in the *rotating* frame of reference, $i = \sqrt{-1}$, T is time, $\omega^* > 0$, $n = 0, 1, 2, \ldots$, and either the plus or minus sign is chosen. $F(R)$ describes any physically realizable deflection (i.e., $F(0) = 0$ for $n > 0$, etc.).

We adopt dimensionless variables (lower case) by normalizing with respect to R_o and Ω and use the cylindrical, rotating co-ordinates (r, θ, z). Using symmetry, we restrict the domain to the quadrant $0 \leqslant r < \infty$ and $0 \leqslant z < \infty$. The dimensionless, inviscid, incompressible Navier–Stokes equations written in the rotating frame of reference, linearized about rigid body rotation are [13]

$$v_{r,t} - 2v_\theta = -p_{,r}, \quad v_{\theta,t} + 2v_r = -p_{,\theta}/r, \quad v_{z,t} = -p_{,z}, \tag{2–4}$$

where v_r, v_θ, v_z, and p are the fluid velocities and pressure, and a comma indicates partial differentiation. Continuity requires

$$v_{r,r} + v_r/r + v_{\theta,\theta}/r + v_{z,z} = 0. \tag{5}$$

The dimensionless boundary conditions for the problem are

$$v_z = \mathrm{e}^{\mathrm{i}(\omega t \pm n\theta)} f(r) \quad \text{on } z = 0,\ r < 1, \qquad p = 0 \quad \text{on } z = 0,\ r > 1. \tag{6, 7}$$

As $r^2 + z^2 \to \infty$ we either require the solution to be bounded or impose a radiation condition depending on whether the system equations are elliptic or hyperbolic respectively.

The problem is solved by substituting the separable forms

$$v_r = \mathrm{e}^{\mathrm{i}(\omega t \pm n\theta)} u_r(r, z), \quad v_\theta = \mathrm{e}^{\mathrm{i}(\omega t \pm n\theta)} u_\theta(r, z), \qquad v_z = \mathrm{e}^{\mathrm{i}(\omega t \pm n\theta)} u_z(r, z),$$

$$p = -\mathrm{i}\omega \mathrm{e}^{\mathrm{i}(\omega t \pm n\theta)} \phi(r, z) \tag{8}$$

into equations (24)–(26) and solving for u_r, u_θ, and u_z in terms of ϕ. This gives

$$u_r = \frac{\omega}{\omega^2 - 4} \left(\omega \phi_{,r} + \frac{n}{r} \phi \right), \tag{9}$$

$$u_\theta = \frac{-\mathrm{i}\omega}{\omega^2 - 4} \left(\phi_{,r} + \frac{n\omega}{r} \phi \right), \qquad u_z = \phi_{,z}. \tag{10, 11}$$

Substitution of equations (9)–(11) into equation (5) then gives the governing equation

$$\nabla^2 \phi - \frac{4}{\omega^2} \phi_{,zz} = 0 \tag{12}$$

provided $\omega \neq 2$. Equation (12) is elliptic for $\omega > 2$ and hyperbolic for $\omega < 2$. ($\omega = 2$ is the point at which the convective acceleration of the rotating fluid—the 2′s in equations (2) and (3)—become "small" compared to the forced oscillation.) Boundary conditions (6) and (7) reduce to

$$\phi_{,z} = f(r) \quad \text{on } z = 0, \quad r < 1, \qquad \phi = 0 \quad \text{on } z = 0, \ r > 1. \tag{13, 14}$$

Application of the Hankel transform solution technique to equation (12) gives [14]

$$\phi = \begin{cases} -\alpha^{-1} \displaystyle\int_0^\infty A(u) \mathrm{e}^{-\alpha z u} J_n(ru)\, \mathrm{d}u, & \omega > 2, \ \alpha = (1 - 4/\omega^2)^{-1/2}, \\ \beta^{-1} \displaystyle\int_0^\infty A(u) [\sin(\beta z u) + \mathrm{i} \cos(\beta z u)] J_n(ru)\, \mathrm{d}u, & \omega < 2, \ \beta = (4/\omega^2 - 1)^{1/2}, \end{cases} \tag{15}$$

where $A(u)$ is a function to be determined. For $\omega > 2$, the exponentially decaying solution is chosen in order to bound the solutions for large r nd z. For $\omega < 2$, the term $\exp(-\mathrm{i}\beta z u)$ is chosen because it gives wave solutions travelling away from the disk when combined with $\exp(\mathrm{i}\omega t \pm \mathrm{i}n\theta)$, which satisfies the radiation condition. Boundary conditions (13) and (14) reduce to the dual integral equations

$$\int_0^\infty u A(u) J_n(ru)\, \mathrm{d}u = f(r) \quad \text{for } r < 1, \tag{16}$$

$$\int_0^\infty A(u) J_n(ru)\, \mathrm{d}u = 0 \quad \text{for } r > 1. \tag{17}$$

The solution of equations (16) and (17) is given by Sneddon [14]:

$$A(u) = \left(\frac{2u}{\pi}\right)^{1/2} \int_0^1 s^{3/2} J_{n+1/2}(us)\, \mathrm{d}s \int_0^1 (1 - \xi^2)^{-1/2} \xi^{1+n} f(s\xi)\, \mathrm{d}\xi. \tag{18}$$

When $f(r)$ is a polynomial, $A(u)$ is easily calculated from equation (18) and takes the form of a sum of integral powers of u multiplied by 1, $\sin(u)$ and $\cos(u)$. When this result is substituted into equation (15), however, the infinite integral is characterized by slowly decaying oscillations and can be difficult to accurately calculate numerically. For $\omega > 2$, ϕ can be expanded into a sum of integrals of the Weber/Schafheitlin type, and the resulting integrals can be calculated using the formulas given in Watson [15]. For large z, the integrals may even be calculated by direct numerical integration.

For $\omega < 2$, evaluation of ϕ is more difficult. If the formula for ϕ is expanded directly into a sum of Weber/Schafheitlin integrals, many of these individual integrals fail to converge even though the sum converges. For instance, for the rigid disk case $n = 0$ and $f = 1$,

$$A = (2/\pi)^{1/2} u^{-1/2} J_{3/2}(u) = (2/\pi) [u^{-2} \sin(u) - u^{-1} \cos(u)]. \tag{19}$$

In this case, the power series expansion about $u = 0$ for each of the terms on the right-hand side of equation (19) starts with the term u^{-1}, whereas the expansion of their sum starts with u. This problem is even more acute for the derivatives of ϕ.

Compounding this difficulty is the fact that ϕ may be discontinuous at particular values of r and z when $\omega < 2$. From the form of the Weber/Schafheitlin integrals, we deduce that ϕ may be discontinuous across the lines

$$r = \pm 1 \pm \beta z, \tag{20}$$

which are the two characteristics of the hyperbolic equation (12) emanating from the rim of the disk [13].

For the special case in which the disk deflection takes the form

$$f(r) = r^{n+2p}, \tag{21}$$

where $p = 0, 1, 2, \ldots,$ formula (18) can be integrated by parts, and $A(u)$ written as a sum of Bessel functions. For example,

$$A(u) = \begin{cases} (2/\pi)^{12/2} a_{n0} u^{-1/2} J_{n+3/2}(u), & p = 0, \\ (2/\pi)^{1/2} a_{n1} [u^{-1/2} J_{n+3/2}(u) - 2u^{-3/2} J_{n+5/2}(u)], & p = 1, \\ (2/\pi)^{1/2} a_{n2} [u^{-1/2} J_{n+3/2}(u) - 4u^{3/2} J_{n+5/2}(u) + 8u^{-5/2} J_{n+7/2}(u)], & p = 2, \end{cases} \tag{22}$$

where a_{np} are constants. For equation (22), ϕ can be written as the integral of a product of three Bessel functions. Watson [15, section 13.46, equation (7)] gives a formula for such integrals. This solution method does not converge on (and close to) the discontinuities. Greenspan [13] uses the formulas given in Erdelyi [16, in particular, Fourier sine transform formula (29)]. These formulas only appear to work for $p = 0$.

A more satisfactory and general method of computing ϕ is to reverse the order of integration. The formula for ϕ is rewritten as

$$\phi = 2^{1/2} \pi^{-1/2} \beta^{-1} \int_0^1 (1 - \xi^2)^{-1/2} \xi^{1+n} \, \mathrm{d}\xi$$

$$\times \int_0^1 s^{3/2} f(s\xi) \, \mathrm{d}s \int_0^\infty u^{1/2} [\sin(\beta z u) + \mathrm{i} \cos(\beta z u)] J_{n+1/2}(us) J_n(ru) \, \mathrm{d}u. \tag{23}$$

The products of $\sin(\beta z u)$ and $\cos(\beta z u)$ with $J_{n+1/2}(us)$ are expanded into a sum of sines and cosines, and each of these, multiplied by $J_n(ru)$, is evaluated as a special case of the Weber/Schafheitlin integral. These integrals always exist. The two finite integrals are then integrated using numerical quadrature. This solution method appears to work well for any physically meaningful $f(r)$. We note, however, that this method only works for evaluating ϕ; when evaluating its derivatives, the Weber/Schafheitlin integrals do not converge.

Table 1 compares the exact solution for $\mathrm{Re}[\phi]$ to the approximate solutions computed by reversing the order of integration and the triple Bessel function formula for two special cases in which the exact solution can be computed using [16]: $n = 0$, $f = 1$, $\beta = 1$, $\mathrm{Re}[\phi] = z$ for $0 < z < 1 - r$; and $n = 1$, $f = r$, $\beta = 1$, $\mathrm{Re}[\phi] = rz$ for $0 < z < 1 - r$. A number of different values of r and z are shown. Both methods work well and have errors less than 1% in all cases.

Figure 1 show contour plots of the real and imaginary parts of ϕ for $f = r^2$ for $n = 0$ computed using the reversed integration method. The discontinuities in ϕ across the characteristics $1 \pm \beta z$ are clearly visible for both the real and imaginary parts of ϕ. The overall pattern of the contours is similar to the steamlines for the rigid disk case [13]. A few contour lines are wavy due to errors in the calculation procedure. These errors are small.

TABLE 1

Comparison of calculation methods for ϕ

		Exact	Reversed integration		Triple Bessel function	
r	z	ϕ	ϕ	% Error	ϕ	% Error
Case 1: $n = 0, f(r) = 1, \beta = 1, \mathrm{Re}[\phi] = z$ *for* $0 < z < 1 - r$						
0·1	0·1	0·10	0·10037178	0·37	0·09997366	− 0·03
0·1	0·3	0·30	0·30111533	0·37	0·29990030	− 0·03
0·1	0·5	0·50	0·50185888	0·37	0·50056211	0·11
0·1	0·7	0·70	0·70260243	0·37	0·69904215	− 0·14
0·3	0·1	0·10	0·09935658	− 0·64	0·09999508	0·00
0·3	0·3	0·30	0·30111533	0·37	0·30001764	0·01
0·3	0·5	0·50	0·50185888	0·37	0·49963110	− 0·07
0·5	0·1	0·10	0·10001674	0·02	0·10001457	0·01
0·5	0·3	0·30	0·30105522	0·35	0·29959208	− 0·14
0·7	0·1	0·10	0·09969257	− 0·31	0·10022353	0·22
Case 2: $n = 1, f(r) = r, \beta = 1, \mathrm{Re}[\phi] = rz$ *for* $0 < z < 1 - r$						
0·1	0·1	0·01	0·00997238	− 0·28	0·01000863	0·09
0·1	0·3	0·03	0·02991715	− 0·28	0·03003920	0·13
0·1	0·5	0·05	0·04986192	− 0·28	0·04998550	− 0·03
0·1	0·7	0·07	0·06980669	− 0·28	0·07031714	0·45
0·3	0·1	0·03	0·02983788	− 0·54	0·03001646	0·05
0·3	0·3	0·09	0·08975146	− 0·28	0·09008443	0·09
0·3	0·5	0·15	0·14958577	− 0·28	0·15039635	0·26
0·5	0·1	0·05	0·04976574	− 0·47	0·04992356	− 0·15
0·5	0·3	0·15	0·15109641	0·73	0·14978147	− 0·15
0·7	0·1	0·07	0·06961352	− 0·55	0·07007755	0·11

3. RELEVANCE TO AEROELASTIC FLUTTER

The problem solved in the previous section is a classical one and the results for the rigid disk have been known for decades. The extension of these classical results to include flexible disks and the different evaluation procedures are new contributions of this paper. Our primary interest, however, is the possible relevance of this problem to the aeroelastic flutter problem.

Experimental data on different rotating disks undergoing aeroelastic flutter have indicated that the Mach number of the rim of the disk is an important parameter for determining the onset of flutter even though the Mach numbers are small [3]. One possible explanation for the importance of the Mach numbers which is suggested by section 2 is the existence of compressible boundary layers in the flow. Such boundary layers could exist in the neighborhood of discontinuous, incompressible flow fields such as those described here. The problem studied here with its steady, rigid body rotation is similar to the conditions found near a rim of a rotating disk. Consequently, it is plausible that the flow field near the rim of an actual rotating disk possesses discontinuous flow fields modulated by compressible boundary layers.

In the problem solved in the previous section, discontinuities only occur for flutter frequencies less then twice the rotation speed of the disk. Although flutter frequencies are not reported for all the experimental data in reference [2, 3], three data points can be determined. For the steel disk reported in reference [2], the ratio of the flutter frequency to

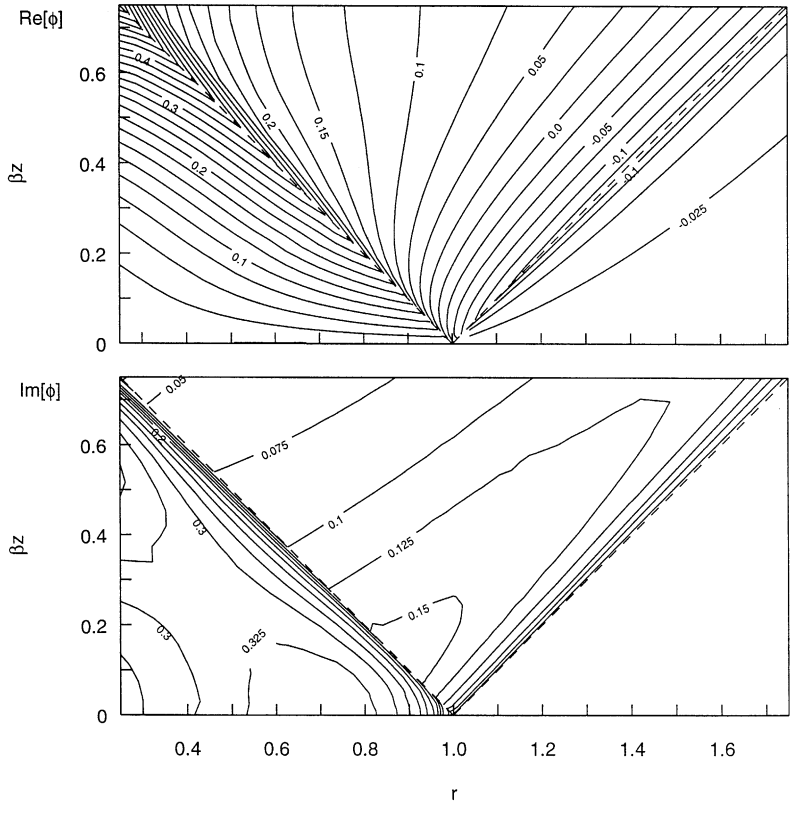

Figure 1. Contour plot of $\mathrm{Re}[\phi]$ (top) and $\mathrm{Im}[\phi]$ (bottom) for $n = 0$ and $f(r) = r^2$. Characteristics emanating from the disk edge are shown by the ---- line. $\mathrm{Im}[\phi] = 0$ below the characteristic $r = 1 + \beta z$.

the rotation speed in two cases is 0·47 and 0·62; for the oak tag disk reported [3], the ratio is 0·24 in one case. The fact that these flutter frequencies are less than two gives circumstantial support of the relevance of the problem studied in the previous section to aeroelastic flutter.

4. AEROELASTIC FLUTTER: PHYSICAL MODELLING AND DIMENSIONAL ANALYSIS

We now turn our attention to a predictive model for aeroelastic flutter. At the risk of confusion, we change to a stationary frame of reference for this analysis, rather than the co-rotating frame of reference adopted in section 2.

A thin, axisymmetric, circular disk of radius R_o spins about its axis of symmetry at a constant angular speed Ω. The disk is surrounded by an unbounded, compressible fluid of density ρ_f and acoustic velocity a. *Stationary*, cylindrical co-ordinates (R, θ, Z) are adopted with the center of the disk at the origin and the undeflected disk lying in the $Z = 0$ plane. The disk is rigidly clamped between $0 \leqslant R \leqslant R_i$ and unsupported between $R_i \leqslant R \leqslant R_o$. The disk is of uniform thickness H, flexural rigidity D, density ρ_d, and the Poisson ratio ν. $W(T, R, \theta)$ is the transverse displacement of the disk in the positive Z direction where T is time, $\sigma_r^*(R)$ and $\sigma_\theta^*(R)$ are the in-plane radial and hoop stresses created by rotation, and $Q(T, R, \theta)$ is the transverse load per unit area in the positive Z direction.

We wish to predict the stability of steady rotation. The linearized equation of the motion for the disk about the equilibrium $W = 0$ written in the stationary frame of reference [17] is

$$\rho_d H(W_{,TT} + 2\Omega W_{,T\theta} + \Omega^2 W_{,\theta\theta}) = Q - D\nabla^4 W + \frac{H}{R}(R\sigma_R^* W_{,R})_{,R} + \frac{H}{R^2}\sigma_\theta^* W_{,\theta\theta}, \quad (24)$$

where comma indicates partial differentiation.

The steady fluid motions are generated by viscous drag on the disk [18]. However, in order to derive the flow's dependence on dimensionless parameters, consider the following thought experiment: suppose that both the steady and perturbed fluid motions can be modelled using irrotational flow fields. Characterize the steady viscous flow by the flow field $V_o(R, Z)$ and model the small, compressible fluid velocity deviations from steady state using a velocity potential Φ such that the perturbed fluid velocity V is given by

$$V = \nabla\Phi. \quad (25)$$

The velocity potential is then governed by [19]

$$\nabla^2\Phi = \frac{1}{a^2}\left(\frac{\partial}{\partial T} + V_o\cdot\nabla\right)^2\Phi. \quad (26)$$

Equations (24) and (26) are coupled on the disk surface though the fluid pressure

$$Q = -(P|_{Z=0^+} - P|_{Z=0^-}) = \rho_f(\Phi_{,T}|_{Z=0^+} - \Phi_{,T}|_{Z=0^-}) \equiv \rho_f[\Phi_{,T}]$$
$$\text{for } R \leqslant R_o,\ Z = 0 \quad (27)$$

and velocity matching:

$$W_{,T} = V_z \quad \text{for } R \leqslant R_o, \quad Z = 0. \quad (28)$$

Symmetries of the problem provide the pressure boundary condition

$$P = 0 \quad \text{for } R > R_o, \quad Z = 0. \quad (29)$$

Dimensionless variables are defined by

$$r = R/R_o, \quad z = Z/R_o, \quad t = T\Omega,$$
$$w = W/H, \quad v = V/(\Omega H), \quad \phi = \Phi/(\Omega R_o H),$$
$$q = Q/(\rho_d\Omega^2 H^2), \quad \sigma_r = \sigma_r^*/(\rho_d\Omega^2 R_o^2), \quad \sigma_\theta = \sigma_\theta^*/(\rho_d\Omega^2 R_o^2). \quad (30)$$

With these definitions, equation (24) becomes

$$w_{,tt} + 2w_{,t\theta} + w_{,\theta\theta} = \Lambda[\phi_{,t}] - \varepsilon\nabla^4 w + (r\sigma_r w_{,r})_{,r}/r + \sigma_\theta w_{,\theta\theta}/r^2, \quad (31)$$

equation (26) becomes

$$\nabla^2\phi = M^2\left(\frac{\partial}{\partial t} + v_o\cdot\nabla\right)^2\phi, \quad (32)$$

and equation (28) becomes

$$\phi_{,z} = w_{,t}, \quad 0 \leqslant r \leqslant 1, \quad z = 0, \quad (33)$$

with the understanding that $w \equiv 0$ for $0 \leqslant r \leqslant \kappa$. Equation (29) becomes

$$\phi_{,t} = 0, \quad r > 1, \quad z = 0. \tag{34}$$

The disk satisfies clamped-free boundary conditions:

$$w = w_{,r} = 0 \quad \text{at } r = \kappa, \tag{35}$$

$$w_{,rr} + \nu(w_{,r}/r + w_{,\theta\theta}/r^2) = 0 \quad \text{at } r = 1, \tag{36}$$

$$(\nabla^2 w)_{,r} + (1 - \nu)(w_{,r\theta\theta}/r^2 - w_{,\theta\theta}/r^3) = 0 \quad \text{at } r = 1. \tag{37}$$

The farfield boundary conditions on ϕ are vanishing fluid velocity as $r^2 + z^2 \to \infty$.

The dimensionless parameters used in equations (31)–(37) are the clamping ratio,

$$\kappa = R_i/R_o, \tag{38}$$

the ratio of the bending stiffness of the disk to the stiffness derived from centrifugal forces,

$$\varepsilon = D/\rho_d \Omega^2 H R_o^4, \tag{39}$$

the fluid/disk density ratio,

$$\Lambda = \rho_f R_o/(\rho_d H), \tag{40}$$

and the Mach number of the outer edge of the disk,

$$M = R_o \Omega/a. \tag{41}$$

For a fixed disk geometry and acoustic velocity, the parameter combination εM^2 remains constant for all Ω and ρ_f. For a fixed disk material, acoustic velocity, and ρ_f, the combination of $\varepsilon M^2 \Lambda^2$ remains constant for all R_o and H.

The in-plane stresses satisfy the generalized plane-stress equations of linear elasticity with a centrifugal body force, zero in-plane displacement at $r = \kappa$, and zero traction along $r = 1$ [20]:

$$\sigma_r = b_0/r^2 + b_1 + b_3 r^2, \qquad \sigma_\theta = -b_0/r^2 + b_1 + b_4 r^2, \tag{42}$$

where

$$b_0 = \frac{\kappa^2(1 - \nu)[3 + \nu - (1 + \nu)\kappa^2]}{8[1 + \nu + (1 - \nu)\kappa^2]}, \quad b_1 = \frac{(1 + \nu)[3 + \nu + (1 - \nu)\kappa^4]}{8[1 + \nu + (1 - \nu)\kappa^2]},$$

$$b_3 = -(3 + \nu)/8, \qquad b_4 = -(1 + 3\nu)/8. \tag{43}$$

5. MATHEMATICAL SIMPLIFICATION

The model presented in the previous section is incomplete because we have not specified the steady state flow field v_o nor justified how it can describe a viscosity-driven flow. Nevertheless, we use the model as a starting point for developing a simpler mathematical model. For $M^2 \ll 1$ the right-hand side of equation (32) is negligible except in the vicinity of boundary layers, i.e., the fluid behaves as an incompressible, perfect fluid with $M = 0$. Experimental results indicate that M is important for predicting aeroelastic flutter even

though typically $M < 0{\cdot}3$ [3]. Consequently, we postulate the presence of a compressible boundary layer near the rim of the disk.

We adopt a simplified, mathematical model for the compressible boundary layer at the rim of the disk by transferring the effects of compressibility from equation (32) to the boundary conditions. We replace equation (32) with Laplace's equation,

$$\nabla^2 \phi = 0, \tag{44}$$

and boundary condition (33) with

$$\phi_{,z} = w_{,t}[1 + M^2 h(r, \varepsilon)], \quad 0 \leqslant r \leqslant 1, \ z = 0, \tag{45}$$

where $h(r, \varepsilon)$ is a weighting function describing the strength of the boundary layer by imposing an artificial transverse velocity to the fluid. Since the boundary layer is expected to be localized near the rim of the disk, $h(r, \varepsilon)$ is small everywhere except near the rim of the disk. The explicit M^2 dependence is retained from the right-hand side of equation (32) while the dependence on ε is simply assumed. Boundary condition (34) remains unchanged.

Our objective here is to develop a simple, predictive model. We plan to determine $h(r, \varepsilon)$ by fitting the flutter results of model (45) to known experimental data. With $h(r, \varepsilon)$ then fixed, we can then predict aeroelastic flutter for different experimental parameters.

The transfer of compressibility from the fluid equation (32) to the boundary conditions (45) is, admittedly, *ad hoc*. However, this transfer has the great advantage of rendering the resulting problem soluble. This is of paramount importance in our goal of constructing a predictive model.

6. NUMERICAL SOLUTION

We seek separable solutions of the form

$$w = u(r)\, \mathrm{e}^{\mathrm{i}\omega t \pm \mathrm{i}n\theta}, \qquad \phi = \mathrm{i}\omega\psi(r)\, \mathrm{e}^{\mathrm{i}\omega t \pm \mathrm{i}n\theta}, \tag{46}$$

where $n = 0, 1, 2, \ldots$ and either the plus or minus sign is chosen. ϕ is antisymmetric about $z = 0$ so we need only determine ϕ for $z > 0$ and can replace $[\phi_{,t}]$ by $2\mathrm{i}\omega\phi$. The fluid problem reduces to

$$\nabla_n^2 \psi = 0, \tag{47}$$

where ∇_n^2 is the Laplacian with n nodal diameters subject to the mixed boundary conditions

$$\psi_{,z} = [1 + M^2 h(r, \varepsilon)]\, u(r) \quad \text{for } r < 1, \ z = 0, \tag{48}$$

$$\psi = 0 \quad \text{for } r > 1, \ z = 0. \tag{49}$$

Equations (47)–(49) are a classical problem whose solution is given by Sneddon [14]. We discretize $u(r)$ with the finite-dimensional approximation

$$u(r) = \sum_{k=1}^{N} c_k f_k(r), \tag{50}$$

where the $f_k(r)$ are linearly independent polynomials satisfying homogenous boundary conditions (35)–(37) and orthonormal with respect to the inner product

$$\langle a, b\rangle = \int_\kappa^1 abr\,\mathrm{d}r. \tag{51}$$

The vibration frequencies ω are determined using Galerkin's method, which reduces to the real, quadratic eigenvalue problem

$$\omega^2(I - 2\Lambda P - 2\Lambda M^2 D) \pm 2n\omega I - \varepsilon K_b + K_\sigma = 0, \tag{52}$$

where the matrices I, P, D, K_b and K_σ are defined by the inner products

$$I_{ij} = \langle f_j, f_i\rangle = \delta_{ij}, \qquad P_{ij} = \langle S[f_j], f_i\rangle, \tag{53, 54}$$

$$D_{ij} = \sum_{k=1}^{N} \langle hf_j, f_k\rangle \langle S[f_k], f_i\rangle, \qquad (K_b)_{ij} = \langle \nabla_n^4 f_j, f_i\rangle, \tag{55, 56}$$

$$(K_\sigma)_{ij} = \langle (r\sigma_r f_{j,r})_{,r}/r - n^2(\sigma_\theta/r^2 - 1) f_j, f_i\rangle, \tag{57}$$

and the linear operator $S[\,\cdot\,]$ is given by [14]

$$S[f_j] = \frac{2r^n}{\pi} \int_r^1 \frac{x^{-2n}\,\mathrm{d}x}{(x^2 - r^2)^{1/2}} \int_\kappa^x \frac{s^{n+1} f_j(s)\,\mathrm{d}s}{(x^2 - s^2)^{1/2}}. \tag{58}$$

Stability requires $\mathrm{Im}[\omega] \geqslant 0$. For given n, κ, ε, and M, a numerical root finder is used to determine the lowest value of Λ at which $\mathrm{Im}[\omega] < 0$ first occurs. If (ω, n) is a solution, then $(-\omega, -n)$ is also a solution; therefore, it is sufficient to let $n = 0, 1, 2, \ldots$ The lowest value over all n gives the stability boundary for the disk/fluid system.

7. EMPIRICAL DATA

The unknown parameter of our model, the boundary layer weighting function $h(r, \varepsilon)$, is to be chosen using experimental data. For simplicity, we restrict ourselves to $\kappa = 0{\cdot}3$. We divide our data set into two groups. In the first group, listed in Table 2, the data is reliable and the effects of enclosures and surfaces close to the rotating disk may be neglected. In the second group, listed in Table 3, either the data has a large amount of scatter or enclosure effects are significant. Tables 2 and 3 list experimental parameters, flutter speed $\Omega_{flutter}$, number of nodal diameters n, and dimensional flutter frequency $\omega_{flutter}$.

D'Angelo and Mote [2] report flutter measurements for a steel disk in different fluid pressures. The manner in which the experiments were performed suggests that this data is accurate and reliable. However, the effect of the vacuum chamber on these experiments appears to be substantial. In these experiments, the radius of the disk is 0·178 m, but the radial clearance with the vacuum chamber is only 2·5 cm. As a result, the flutter speed is 3500 rpm at atmospheric pressure in the absence of any enclosure but only 2800 rpm at atmospheric pressure when in the vacuum chamber, a reduction of 20%. Using the apparatus described below, the authors were able to change the measured flutter speed of a 0·151 m radius, aluminium disk by $+12\%$ to -12% depending on the disk thickness by enclosing the disk in a 0·171 m radius cylindrical shroud. For our modelling here, we list the one, unenclosed data point measured by reference [2] as the first data point listed in Table 2

TABLE 2

Reliable experimental flutter data for unshrouded disks with $\kappa = 0{\cdot}3$

Datum	R_o (m)	H (mm)	ρ_f (kg/m^3)	$\Omega_{flutter}$ (rpm)	n	$\omega_{flutter}$ (Hz)
Data for the steel disk reported in reference [2]						
1	0·178	0·775	1·09	3500	3	34
Data for the oak tag disk reported in reference [3]						
2	0·148	0·279	0·04	4143	—	—
3	0·148	0·279	0·08	3705	—	—
4	0·148	0·279	0·10	3313	—	—
5	0·148	0·279	0·10	2904	—	—
6	0·148	0·279	0·13	2995	—	—
7	0·148	0·279	0·16	2625	—	—
8	0·148	0·279	0·22	2348	—	—
9	0·148	0·279	0·24	2076	—	—
10	0·148	0·279	0·34	2036	—	—
11	0·148	0·279	0·42	1712	—	—
12	0·148	0·279	0·53	1712	—	—
13	0·148	0·279	0·67	1712	—	—
14	0·148	0·279	1·17	1414	—	—
15	0·148	0·279	1·17	1804	—	—
Data for the aluminum disks measured here						
16	0·151	0·406	1·09	2400	—	12
17	0·151	0·483	1·09	2500	—	13
18	0·151	0·610	1·09	3800	—	23
19	0·151	0·775	1·09	4650	—	34
20	0·151	0·991	1·09	5600	—	52
21	0·151	1·245	1·09	7180	—	66
22	0·191	0·406	1·09	1900	—	9
23	0·191	0·495	1·09	1810	—	11
24	0·191	0·635	1·09	2100	—	14
25	0·191	0·787	1·09	2600	—	20
26	0·191	0·978	1·09	3350	—	30
27	0·191	1·245	1·09	4500	—	42
28	0·191	1·575	1·09	6000	—	62

and the other data points for which the enclosure is significant as data points 29–36 in Table 3.

Renshaw *et al.* [3] report flutter measurements for oak tag and vellum disks taken in the same vacuum chamber used by reference [2]. A radial clearance of one to five disk radii is reported for these measurements. We assume that this clearance is sufficient to eliminate any enclosure effects. The relative error in the oak tag measurements is reasonable (roughly 20%). However, the scatter in the vellum data is substantial (300%, or so). We therefore assign a sampling of 14 oak tag data points to Table 2 and a sampling of 23 vellum data points to Table 3. These data points were determined by scanning the plots shown in reference [3]; as a result, these points have small errors associated with their measurement off the scanned plots.

In order to supplement these data points, a set of flutter speeds were measured by the authors for 0·151 and 0·191 m radius aluminum disks of thickness ranging from 0·406 to 1·575 m. These disks were spun in air at atmospheric pressure at different speeds using

TABLE 3

Suspect experimental flutter data for disks with $\kappa = 0{\cdot}3$

Datum	R_o (m)	H (mm)	ρ_f (kg/m^3)	$\Omega_{flutter}$ (rpm)	n	$\omega_{flutter}$ (Hz)
Data for the steel disk reported in reference [2]; *enclosure effect significant*						
29	0·178	0·775	0·0035	8718	3 & 4	—
30	0·178	0·775	0·010	5909	3	—
31	0·178	0·775	0·019	4766	3	—
32	0·178	0·775	0·025	4178	3	—
33	0·178	0·775	0·034	4052	3	—
34	0·178	0·775	0·069	3275	3	—
35	0·178	0·775	0·10	3080	3	—
36	0·178	0·775	0·14	2701	3	—
Data for the vellum disk reported in reference [3]; *significant scatter in data*						
37	0·148	0·0635	0·064	2995	—	—
38	0·148	0·0635	0·089	2649	—	—
39	0·148	0·0635	0·13	2421	—	—
40	0·148	0·0635	0·094	1488	—	—
41	0·148	0·0635	0·060	1427	—	—
42	0·148	0·0635	0·12	1301	—	—
43	0·148	0·0635	0·16	1628	—	—
44	0·148	0·0635	0·23	1164	—	—
45	0·148	0·0635	0·20	959	—	—
46	0·148	0·0635	0·20	745	—	—
47	0·148	0·0635	0·27	850	—	—
48	0·148	0·0635	0·31	775	—	—
49	0·148	0·0635	0·39	784	—	—
50	0·148	0·0635	0·49	715	—	—
51	0·148	0·0635	0·54	817	—	—
52	0·148	0·0635	0·59	693	—	—
53	0·148	0·0635	0·80	752	—	—
54	0·148	0·0635	1·00	752	—	—
55	0·148	0·0635	1·00	615	—	—
56	0·148	0·0635	1·02	544	—	—
57	0·148	0·0635	1·00	1342	—	—
58	0·148	0·0635	0·67	1075	—	—
59	0·148	0·0635	0·52	1262	—	—

a brushless DC motor. The transverse vibrations at a single, spatially fixed location were measured using a Philtec photonic sensor with a sensitivity of 0·0001 m/V. At each speed, 7 s of data was acquired at 2048 Hz. The rms deviation of this reading from its average value determined the magnitude of transverse vibration and a power spectrum of the data determined the vibration frequencies. Figure 2 shows a typical plot of transverse vibration magnitude versus rotation speed for a 0·151 m radius, 0·775 mm thick disk. Initially, the transverse vibration magnitude decreases with rotation speed due to the centripetal flattening of the initial run out of the disk. Above flutter, however, the vibration magnitude increases rapidly for small increases in rotation speed. The flutter speeds and frequencies of these measurements are reported in Table 2 as data points 16–28.

The values of the dimensionless Λ, M, ε, and the dimensionless flutter frequency corresponding to the data in Tables 2 and 3 are given in Tables 4 and 5 respectively. In Table 4, $0{\cdot}0272 \leqslant \Lambda \leqslant 0{\cdot}7111$, $0{\cdot}0811 \leqslant M \leqslant 0{\cdot}3469$, and $5{\cdot}24 \times 10^{-4} \leqslant \varepsilon \leqslant 1{\cdot}57 \times 10^{-2}$.

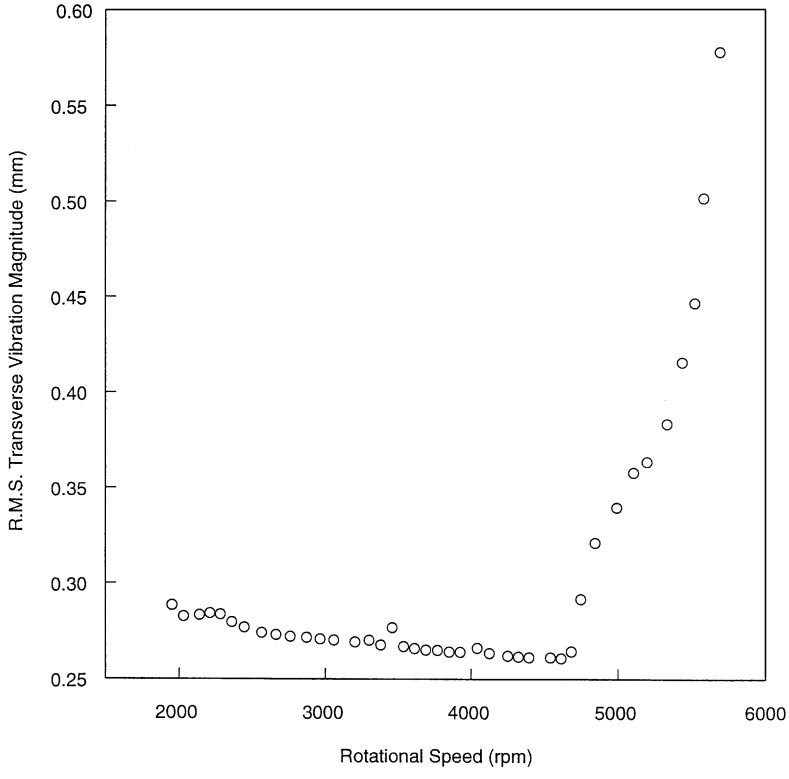

Figure 2. Typical experimental results showing rms vibration amplitude versus rotation speed for a 0·151 m radius, 0·775 mm thick, aluminum disk.

8. DETERMINATION OF $h(r, \varepsilon)$

The unknown parameter of our model, the boundary layer weighting function $h(r, \varepsilon)$, is chosen to minimize the sum of squared, relative errors of the data in Table 4. Initially, we attempted to make the boundary layer weighting function proportional to the Dirac function, $h(r, \varepsilon) = c\delta(r - 1)$. However, these results did not converge as N, the number of trial functions, increased. Consequently, we then investigated polynomial functions as well as exponential dependence on ε. Numerical experiments indicated that the particular choice of the polynomial was not crucial. (This is not surprising since it is weighted by $u(r)$ which is small except near the rim of the disk.) The final form selected was

$$h = -C\varepsilon^{\alpha} r^5 \tag{59}$$

with $N = 8$. For the data in Table 4, the best values of C and α were determined using Powell's method. This gives $C = 2{\cdot}4 \times 10^4$ and $\alpha = 0{\cdot}25$.

Table 6 compares the model's prediction with the data in Table 4 while Table 7 compares the predictions for the data of Table 5. The average absolute value in the percentage error in predicting Λ is 32% for the data of Table 4 and the maximum percentage error is 72%. While these errors are large, they represent a substantial improvement over the predictions of classical aeroelastic theory [3]. The predicted dimensionless flutter frequencies range from 0·86 to 3·39. Where data is available, these overestimate the measured flutter

TABLE 4

Dimensionless flutter parameters for the data given in Table 2

Datum	Λ	M	ε	$\omega_{flutter}/\Omega_{flutter}$
1	0·0326	0·1891	1·10E − 02	0·58
2	0·0272	0·1861	5·24E − 04	—
3	0·0471	0·1664	6·56E − 04	—
4	0·0628	0·1488	8·20E − 04	—
5	0·0628	0·1305	1·07E − 03	—
6	0·0786	0·1345	1·00E − 03	—
7	0·0984	0·1179	1·31E − 03	—
8	0·1333	0·1055	1·63E − 03	—
9	0·1475	0·0933	2·09E − 03	—
10	0·2089	0·0914	2·17E − 03	—
11	0·2559	0·0769	3·07E − 03	—
12	0·3203	0·0769	3·07E − 03	—
13	0·4100	0·0769	3·07E − 03	—
14	0·7111	0·0635	4·50E − 03	—
15	0·7111	0·0811	2·76E − 03	—
16	0·1449	0·1099	1·20E − 02	0·30
17	0·1220	0·1145	1·57E − 02	0·31
18	0·0966	0·1740	1·08E − 02	0·36
19	0·0760	0·2130	1·17E − 02	0·44
20	0·0595	0·2565	1·31E − 02	0·56
21	0·0473	0·3288	1·26E − 02	0·55
22	0·1830	0·1099	7·56E − 03	0·28
23	0·1501	0·1047	1·24E − 02	0·36
24	0·1171	0·1214	1·51E − 02	0·40
25	0·0944	0·1503	1·52E − 02	0·46
26	0·0760	0·1937	1·41E − 02	0·54
27	0·0597	0·2602	1·26E − 02	0·56
28	0·0472	0·3469	1·14E − 02	0·62

frequencies by a factor of two or three. Measurements of the number of nodal diameters of the fluttering mode are only available for the data of reference [2] (data points 1, and 29–36). These predictions are correct except for data point 30; however, the measured data indicates a transition from $n = 3$ to 4 for data point 29 which is similar to data point 30. The errors in predicting Λ for the steel disk in the enclosure are substantially higher than all other data points, being a factor of 2–5 too large. The errors for the vellum disk are within the scatter of these points.

Figures 3 and 4 show plots of the model's predictions against the data of Tables 4 and 5 respectively. The graphs plot M against Λ for either a fixed value of εM^2 (corresponding to a fixed disk geometry at varying ρ_f) or for a fixed value of $\varepsilon M^2 \Lambda^2$ (corresponding to a disk of constant material, constant ρ_f but varying thicknesses and radii). In all cases, the transition curve from stable to unstable vibration is composed of two segments. The first segment is a curve, concave up, from small Λ and high M to large Λ and small M. The second segment is concave down from large Λ to a constant Λ for very small M. The value of the constant Λ corresponds to the classical aeroelasticity result.

Figure 5 shows predicted flutter boundaries for a broad range of εM^2 values. This plot can be used to estimate flutter speeds for different disk designs for $\kappa = 0{\cdot}3$.

TABLE 5

Dimensionless flutter parameters for the data given in Table 3

Datum	Λ	M	ε
29	0·0009	0·4710	1·77E − 03
30	0·0026	0·3193	3·85E − 03
31	0·0051	0·2575	5·91E − 03
32	0·0067	0·2258	7·69E − 03
33	0·0089	0·2189	8·18E − 03
34	0·0180	0·1770	1·25E − 02
35	0·0267	0·1664	1·42E − 02
36	0·0370	0·1459	1·84E − 02
37	0·1706	0·1345	2·93E − 05
38	0·2364	0·1190	3·75E − 05
39	0·3483	0·1087	4·49E − 05
40	0·2514	0·0668	1·19E − 04
41	0·1604	0·0641	1·29E − 04
42	0·3275	0·0585	1·55E − 04
43	0·4266	0·0731	9·94E − 05
44	0·6041	0·0523	1·94E − 04
45	0·5459	0·0431	2·86E − 04
46	0·5224	0·0335	4·74E − 04
47	0·7269	0·0382	3·64E − 04
48	0·8188	0·0348	4·38E − 04
49	1·0479	0·0352	4·28E − 04
50	1·3119	0·0321	5·15E − 04
51	1·4518	0·0367	3·94E − 04
52	1·5716	0·0311	5·47E − 04
53	2·1393	0·0338	4·65E − 04
54	2·6782	0·0338	4·65E − 04
55	2·6782	0·0276	6·97E − 04
56	2·7259	0·0244	8·91E − 04
57	2·6782	0·0603	1·46E − 04
58	1·7779	0·0483	2·28E − 04
59	1·3953	0·0567	1·65E − 04

9. DISCUSSION

9.1. MODELLING

The analytic model investigated here gives a reasonable, order of magnitude estimate of the flutter speed of a disk rotating in an unbounded medium. The data used to generate the model varies widely; as a result, the model's accuracy is only fair. The predicted trends are correct for Λ, the flutter frequency, and the flutter mode. For smaller, less varied sets of data, the model can be fine-tuned substantially. For example, consider just the eight data points 29–36, for which our model gives the worst predictions. The simple model $h = -2{\cdot}9 \times 10^4 r^5$ gives results within 21% for all eight data points.

In our model, the coupled disk/fluid interaction for different kinds of disks is accounted for by the ε dependence in h. We tried to produce a more robust model by altering the analytically derived linear dependence on Λ and quadratic dependence on M shown in equation (52), but these attempts did not produce better predictions. We also tried to produce a more robust model by including a viscous dependence using the Reynolds

TABLE 6

Comparison of theoretical predictions and experimental data of Table 2

Datum	Λ_{theory}	% error in Λ	$\omega_{flutter}$	% error in $\omega_{flutter}$	n
1	0·0497	52	1·13	94	3
2	0·0395	45	3·39	—	5
3	0·0480	2	3·36	—	5
4	0·0588	− 6	3·33	—	5
5	0·0754	20	3·27	—	5
6	0·0712	− 9	3·28	—	5
7	0·0924	− 6	2·49	—	4
8	0·1142	− 14	2·45	—	4
9	0·1463	− 1	2·4	—	4
10	0·1528	− 27	2·39	—	4
11	0·2239	− 12	2·28	—	4
12	0·2239	− 30	2·28	—	4
13	0·2239	− 45	2·28	—	4
14	0·3579	− 50	1·52	—	3
15	0·1982	− 72	2·31	—	4
16	0·1586	− 9	1·07	257	3
17	0·1894	55	0·86	176	3
18	0·0581	− 40	1·14	214	3
19	0·0408	− 46	1·09	148	3
20	0·0307	− 48	1·01	81	3
21	0·0181	− 62	1·04	89	3
22	0·1248	− 32	1·34	371	3
23	0·1796	20	1·05	188	3
24	0·1605	37	0·89	123	3
25	0·1049	11	0·89	93	3
26	0·0580	− 24	0·95	77	3
27	0·0289	− 52	1·04	86	3
28	0·0151	− 68	1·11	79	3
Ave. |error|		32		148	

number of the rim. This also failed to improve the predictions. Although circumstantial, these results support the validity of the model and, in particular, the idea that aeroelastic flutter is driven by a compressible boundary layer near the rim of the disk.

That being said, the analytic derivation of the model could be substantially improved. The steady flow is not irrotational; no-slip conditions are irrelevant in potential flow yet essential to this problem; the pressure is linearized about $v_o = 0$ even though the steady fluid velocity is non-zero; and so on. As emphasized in the introduction, our goal here was a predictive model at the expense of modelling fidelity. The derivation presented here is perhaps best viewed as setting the stage for more refined modelling by identifying a physical mechanism driving aeroelastic flutter and demonstrating that such a mechanism can capture the proper trends observed experimentally.

In contrast to the mechanism proposed here, references [5, 6] propose that flutter is driven by rotating damping forces in the fluid. In addition, they develop an experimental method for predicting flutter by estimating the rotation speed at which a vibration frequency first becomes undamped. In our model, only the mass matrix of the underlying

TABLE 7

Comparison of theoretical predictions and experimental data of Table 3

		% error		
Datum	Λ_{theory}	in Λ	$\omega_{flutter}$	n
29	0·0056	509	2·43	4
30	0·0128	391	2·17	4
31	0·0209	308	1·43	3
32	0·0292	338	1·33	3
33	0·0318	258	1·3	3
34	0·0623	245	1·04	3
35	0·0793	197	0·94	3
36	0·1464	296	0·7	3
37	0·1395	− 18	6·06	8
38	0·1697	− 28	6·05	8
39	0·1967	− 44	6·05	8
40	0·4563	81	5·16	7
41	0·4928	207	5·16	7
42	0·5862	79	5·14	7
43	0·3875	− 9	5·17	7
44	0·7325	21	5·12	7
45	1·1131	104	5·06	7
46	1·8888	262	0	0
47	1·4893	105	5·01	7
48	1·902	132	4·2	6
49	1·844	76	4·2	6
50	1·8505	41	0	0
51	1·6512	14	4·22	6
52	1·8231	16	0	0
53	1·8968	− 11	0	0
54	1·8968	− 29	0	0
55	1·731	− 35	0	0
56	1·6489	− 40	0	0
57	0·5528	− 79	5·15	7
58	0·8645	− 51	5·09	7
59	0·6231	− 55	5·13	7

eigenvalue problem is altered by the fluid, and stable solutions have $\mathrm{Im}(\omega) = 0$, i.e., no damping. These results are therefore at odds with those of references [5, 6].

The most striking aspect of our model, perhaps, is the magnitude of the compressible fluid corrections imposed on the flow. Here, this correction is characterized by the transverse velocity boundary condition (48) and the factor $1 + M^2 h$. For the data in Table 4, this factor ranges from $1 - 25r^5$ to $1 - 944r^5$. In other words, the imposed transverse velocity that accounts for the compressible boundary layer is 180° out of phase and up to three orders of magnitude larger than the actual velocity, at least at the rim of the disk. This corresponds to a large, local change in pressure that is characteristic of shocks and other compressible boundary layers.

9.2. INDUSTRIAL PREDICTIONS

The model described here gives us a "back-of-the-envelope" of whether or not aeroelastic flutter is likely to occur in hard disk drive designs. Table 8 lists design parameters for

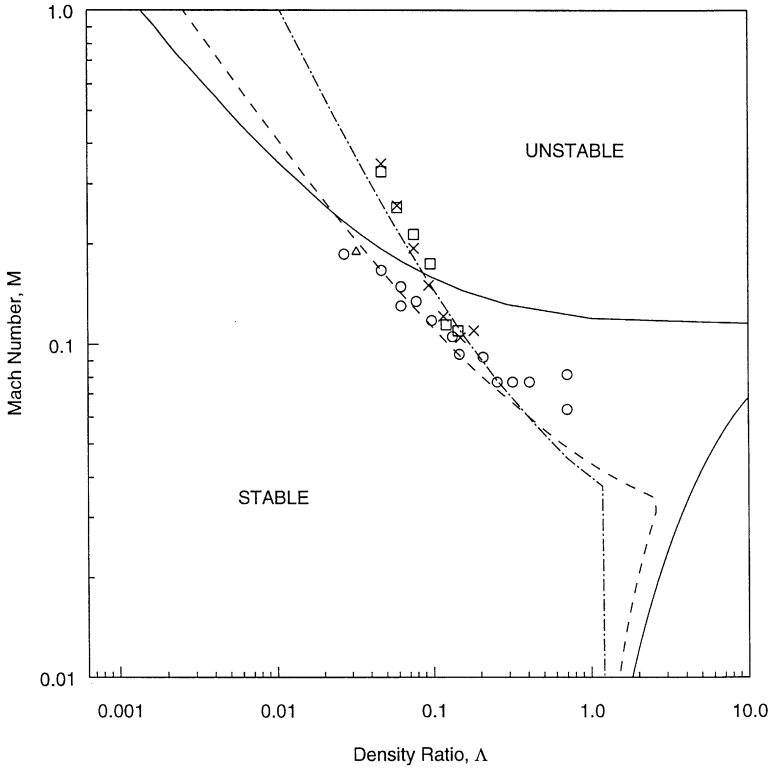

Figure 3. Comparison of the model predictions and experimental data shown in Table 3. Steel: $\varepsilon M^2 = 3{\cdot}92 \times 10^{-4}$, △△, data, ——, theory; oak tag: $\varepsilon M^2 = 1{\cdot}82 \times 10^{-5}$, ○○○, data, - - - - -, theory; aluminum with $R_o = 0{\cdot}151$ m; $\varepsilon M^2 \Lambda^2 = 3{\cdot}05 \times 10^{-6}$, □□, data, ·–·–, theory; aluminum with $R_o = 0{\cdot}191$ m: $\varepsilon M^2 \Lambda^2 = 3{\cdot}05 \times 10^{-6}$, X, data, ·–·–, theory.

TABLE 8

An historical sampling of hard disk drive designs comparing the relative significance of critical speed and flutter speed. All disks are aluminum with $\kappa = 0{\cdot}34$

Year	OD (in)	H (mm)	Ω (rpm)	Fraction of $\Omega_{critical}$ (%)	Fraction of $\Omega_{flutter}$ (%)	M at flutter
1953	24	0·64	360	60·4	34·9	0·10
1973	14	2·54	3600	51·8	44·9	0·43
1980	10	2·03	3600	33·1	29·0	0·48
1980	8	1	3600	43·0	35·5	0·31
1985	5·25	0·8	3600	23·1	19·6	0·37
1990	3·25	0·8	3600	8·9	7·9	0·57
1996	3·25	0·8	7200	17·8	15·9	0·57
2000	3·25	0·8	10000	24·7	22·0	0·57

a number of prototypical disk drive designs produced during the years 1953–2000. Also listed is the fraction of the first critical speed and the fraction of the aeroelastic flutter speed at which these designs operated. (The first critical speed is the lowest speed at which a vibration frequency of the disk vanishes when the disk is uncoupled to air; historically, this

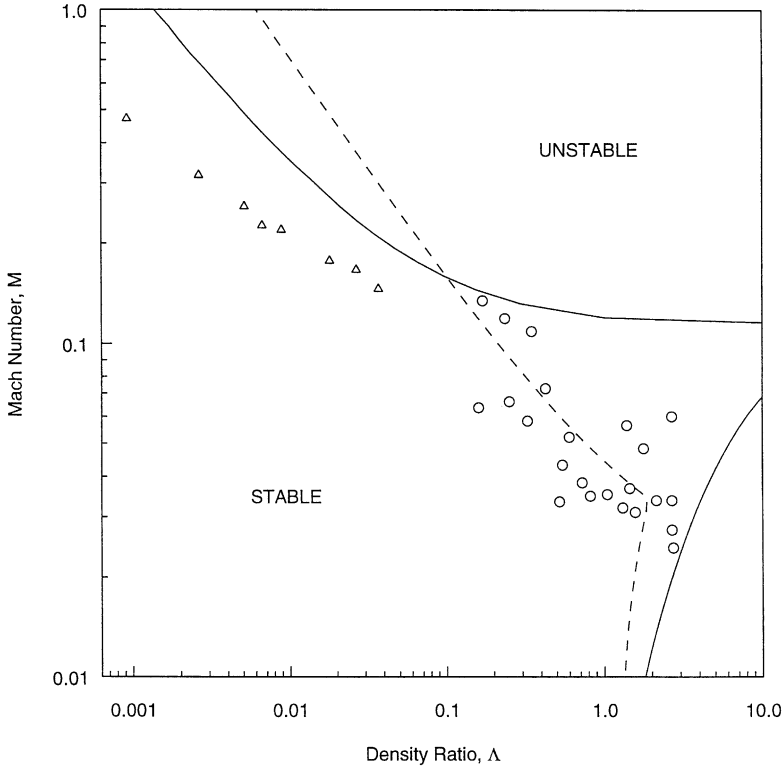

Figure 4. Comparison of the model predictions and experimental data shown in Table 4. Steel: $\varepsilon M^2 = 3{\cdot}92 \times 10^{-4}$, △△, data, ——, theory; vellum: $\varepsilon M^2 = 5{\cdot}31 \times 10^{-7}$, ○○, data, ----, theory.

speed has been a relevant design factor.) Until about 1990, both of these fractions decreased. Since then, however, with the standard 3·25 in design, both fractions are increasing, with current designs operating at about a quarter of the critical and flutter speeds. The rim Mach number required for flutter are substantial and would generally be considered within the compressible range even without boundary layers.

Aeroelastic flutter *per se* will not be an important design driver anytime soon. However, the mechanism that induces flutter is likely to induce unwanted aerodynamically driven vibration of the disk even if the operation speed is well below the flutter speed of the disk. Consequently, an understanding of boundary layer effect near the rim of the disk may be crucial to the next generation of hard disk drives. In addition, enclosure design to reduce such vibration may become industrially important. For example, we predict a flutter speed of 45 000 rpm for an unenclosed 3·5 in disk drive with our model. Kim *et al.* [6] experimentally estimated flutter speeds ranging from 35 000 to 75 000 rpm depending on the enclosure. Such enclosure-induced variations in flutter speed are likely to become important design drivers.

10. CONCLUSIONS

A simple mathematical model is presented for predicting the aeroelastic flutter of a rotating disk in an unbounded fluid. This model is motivated by the solution of a classical

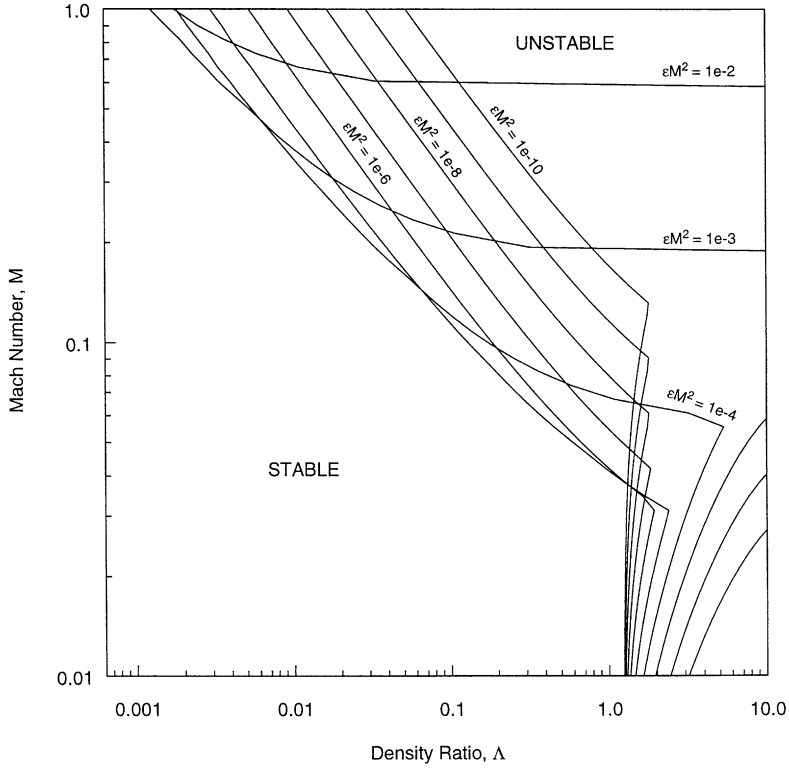

Figure 5. Theoretical flutter predictions for various values of εM^2 for $\kappa = 0{\cdot}3$.

problem, namely the oscillations of a rotating fluid being driven by a co-rotating disk. The solution of this classical model is extended to include flexible disks. A simple model for predicting aeroelastic flutter is proposed. Over a broad range of experimental parameters, the model has the following attributes: (1) flutter speed predictions are within an order of magnitude of experimental data; (2) flutter frequencies are a factor of 2–3 too large; (3) flutter shapes (i.e., nodal diameters, n) are accurate.

The model can be used as a design tool to assess the influence of aeroelastic flutter on potential rotating disk designs. More importantly, the results provide circumstantial evidence for a compressible boundary layer near the rim of a rotating disk with the strength to produce large pressure changes and, consequently, large transverse oscillations. Since large oscillations are generally undesirable, understanding such a boundary layer is essential to their reduction. This investigation sets the stage for more refined modelling efforts aimed at understanding this phenomenon.

REFERENCES

1. Y. M. STAKHEV 1972 *Russian Engineering Journal* **52**, 14–17. Vibrations in thin steel discs.
2. C. D'ANGELO III and C. D. MOTE JR 1993 *Journal of Sound and Vibration* **168**, 15–30. Aerodynamically excited vibration and flutter of a thin disk rotating at supercritical speed.
3. A. A. RENSHAW, C. D'ANGELO III and C. D. MOTE JR 1994 *Journal of Sound and Vibration* **177**, 577–590. Aerodynamically excited vibration of a rotating disk.
4. K. YASUDA, T. TORII and T. SHIMIZU 1992 *JSME International Series III* **35**, 347–352. Self-excited oscillations of a circular disk rotating in air.

5. M. H. HANSEN, A. RAMAN and C. D. MOTE JR 2000 *Journal of Fluids and Structures* (in press). Estimation of non-conservative aerodynamic pressure leading of flutter of spinning disks.
6. B. C. KIM, A. RAMAN and C. D. MOTE JR 2000 *Journal of Sound and Vibration* (in press). Prediction of aeroelastic flutter in a hard disk drive.
7. H. HOSAKA and S. CRANDALL 1992. *Acta Mechanica* **3**, 115–127. Self-excited vibrations of a flexible disk rotating on an air film above a flat surface.
8. A. A. RENSHAW 1998 *Journal of Applied Mechanics* **65**, 116–120. Critical speed for floppy disks.
9. F. Y. HUANG and C. D. MOTE JR 1996 *Journal of Vibration and Acoustics* **118**, 657–662. Mathematical analysis of stability of a spinning disk under rotating, arbitrarily large damping forces.
10. N. GREGORY, J. T. STUART and W. S. WALKER 1955 *Philosophical Transactions of the Royal Society of London, Series A* **248**, 155–199. On the stability of three-dimensional boundary layers with application to the flow due to a rotating disk.
11. M. R. MALIK, S. P. WILKINSON and S. A. ORSZAG 1981 *American Institute of Aeronautics and Astronautics Journal* **19**, 1131–1138. Instability and transition in rotating disk flow.
12. Y. KOHAMA 1984 *Acta Mechanica* **50**, 193–199. Study on boundary layer transition of a rotating disk.
13. H. P. GREENSPAN 1990 *The Theory of Rotating Fluids*. Brookline, Massachuttes: Breukelen Press.
14. I. N. SNEDDON 1996 *Mixed Boundary Value Problems in Potential Theory*. New York: American Elsevier Publishing Co.
15. G. N. WATSON 1944 *A Treatsie on the Theory of Bessel Functions*. Cambridge: Cambridge University Press.
16. A. ERDELYI 1953 *Tables of Integral Transforms*. New York: McGraw-Hill.
17. W. D. IWAN and T. L. MOELLER 1976 *Journal of Applied Mechanics* **43**, 485–490. The stability of a spinning elastic disk with a transverse load system.
18. P. D. ARIEL 1996 *Journal of Applied Mechanics* **63**, 436–438. The flow near a rotating disk: an approximate solution.
19. E. A. DOWELL, H. C. CURTISS JR, R. H. SCANLAN and F. SISTO 1978 *A Modern Course in Aeroelasticity*. Alphen aan den Rijn, The Netherlands: Sijthoff and Noordhoff.
20. I. S. SOKOLNIKOFF 1983 *Mathematical Theory of Elasticity*. Malabar, FL: R. E. Krieger & Co.